



Integratable magnetic shape memory micropump for high-pressure, precision microfluidic applications

A. Saren¹ · A. R. Smith¹ · K. Ullakko¹

Received: 4 January 2018 / Accepted: 7 March 2018 / Published online: 16 March 2018
© Springer-Verlag GmbH Germany, part of Springer Nature 2018

Abstract

Precisely controlling the flow of fluids on a microscopic scale has been a technological challenge in the field of microfluidics. Active microfluidics, where a defined manipulation of the working fluid is necessary, requires active components such as micropumps or microvalves. We report on an optimized design of an integratable, wireless micropump made from the magnetic shape memory (MSM) alloy Ni–Mn–Ga. An external magnetic field generates a shape change in the MSM material, which drives the fluid in a similar fashion as a peristaltic pump. Thus, the pump does not need electrical contacts and avoids the mechanical parts found in traditional pumping technologies, decreasing the complexity of the micropump. With a discrete pumping resolution of 50–150 nL per pumping cycle, which is further scalable, and a pumping pressure well exceeding 2 bar, the MSM micropump is capable of accurately delivering the fluids needed for microfluidic devices. The MSM micropump is self-priming, pumping both liquid and gas, and demonstrates repeatable performance across a range of pumping frequencies. Furthermore, it operates simultaneously as both a valve and reversible micropump, offering superior possibilities compared to existing technologies within the flow rate range of 0–2000 $\mu\text{L}/\text{min}$. Due to its simplicity, this technology can be scaled down easily, which lends itself for future integration into lab-on-a-chips and microreactors for life science and chemistry applications.

Keywords Microfluidic · Micropump · Fluid delivery · Lab-on-a-chip · Magnetic shape memory · Ni–Mn–Ga

1 Introduction

The field of microfluidics has developed rapidly in recent years due to the many advantages of handling fluids in small scale. Such advantages include reduced sample and reagent use, higher sensitivity, shorter processing times and precision dosing of nanoliter volumes. Additionally, microfluidic devices such as micrototal analysis systems (μTAS), point-of-care diagnostics (PoCD) and lab-on-a-chips (LoC) offer increased mobility compared to their laboratory-scale counterparts (Manz et al. 1990; Stone et al. 2004; Whitesides 2006). A driving force for this development is the

sophistication of MEMS technology and their manufacturing methods.

There has been significant research conducted to address the key challenge of fluid handling in microfluidics which has been identified as a microfluidic component that is relatively underdeveloped (Laser and Santiago 2004; Nguyen et al. 2002). There are several different methods for handling fluid, such as capillary flow (Juncker et al. 2002; Zimmermann et al. 2006), acoustic wave (Guttenberg et al. 2005; Wang and Jian 2011) and electrokinetic (Harrison et al. 1991; Webster et al. 2000), as well as piezoelectric (Smits 1990; Sheen et al. 2008) and peristaltic (Berg et al. 2003; Kai et al. 2004; Husband et al. 2004; Jang and Kan 2007; Pečar et al. 2014) micropumps. An ideal fluid handling solution should have the following characteristics: (a) It should be robust and perform reliably. (b) It should be simple with minimal external connections. (c) It should minimize the overall device size. The aforementioned technologies each have their own shortcomings, such as passive check valves, high voltage requirements, dependency on fluid properties, or complicated design and manufacturing. Mechanical parts

Electronic supplementary material The online version of this article (<https://doi.org/10.1007/s10404-018-2058-0>) contains supplementary material, which is available to authorized users.

✉ K. Ullakko
kari.ullakko@lut.fi

¹ Material Physics Laboratory, Lappeenranta University of Technology, Laitaatsillantie 3, 57170 Savonlinna, Finland

found in traditional pumping technologies, such as check valves and flexing diaphragms, significantly increase the complexity of the micropump and make it more difficult to integrate these pumping technologies into the lab-on-a-chip device.

The magnetic shape memory (MSM) alloy Ni–Mn–Ga has a variety of properties that make it an excellent material for microdevice fabrication. Through a process known as twinning, the crystallographic structure of the MSM alloy can be reoriented by converting energy from an applied magnetic field (Ullakko et al. 1996). The material is capable of large (up to 10%) strains from magnetic field-induced stress (Murray et al. 2000; Sozinov et al. 2002), the strain can be precisely controlled (Ullakko and Likhachev 2000; Smith et al. 2014a) and it has a short actuation time (Tellinen et al. 2002; Smith et al. 2014b; Saren et al. 2016). Since this technology is actuated by a magnetic field, the device can be contact-free. This combination of unique properties makes the MSM-technology-based micropump a competitive device that is ideal for integration into LoC and PoCD devices. Furthermore, the MSM micropump has no mechanical parts; the MSM element is the primary component that acts as both the pumping mechanism and the valve.

The micropump based on the MSM alloy Ni–Mn–Ga was first reported by Ullakko et al. (2012). A prototype was later characterized by Smith et al. (2015) and Barker et al. (2016) used the MSM micropump to deliver drugs into the brain of a rat. The main disadvantage of the design concept suggested by Ullakko et al. (2012) and utilized later by Barker et al. (2016) is the insufficient sealing of the fluid channel which manifests itself in rather big flow rate scattering (reaching $\pm 35\%$) at a constant motor speed (Barker et al. 2016). As a result, these pumps would be unstable and work only against small backpressures (unfortunately, no pressure characterization was presented in these papers). In the design characterized by Smith et al. (2015), the MSM element was purposefully surrounded by an elastic sealing, which substantially improved the pumping performance. However, for operation, this design required the pump being placed between two plates that were clamped together with a fixed force. Our further investigations demonstrated that all the pumping characteristics have a strong dependence on the clamping force. This significantly complicates the practical use of this pump as well as limits the integration possibilities into devices with planar architecture. Furthermore, the pressure characterization was done with another pump having much lower flow rate.

During our research, it was revealed that constraining of the MSM element is necessary for long-term stability of the pump. In the present paper, we discuss a refined design that stabilizes the performance of the pump without the need of additional clamping, characterize the bidirectional pumping and pressure capabilities of this design, and demonstrate the

MSM micropump as an effective pumping solution that can be integrated into LoC devices.

2 Materials and methods

2.1 Pump design and assembly

Similar to previous designs, the MSM micropump consists primarily of the MSM element and an elastic material, which seals the fluid channel. In contrast to previous designs, the MSM element in the reported MSM micropump is enclosed in a constraining environment, which limits straining of the MSM element and the elastic materials beyond the original design intentions.

Figure 1a shows a photograph of the top and side view of the MSM micropump. Figure 1b shows a schematic showing the different parts of the design. The primary component, the MSM element (1), is a single crystalline 5M Ni–Mn–Ga sample that has the final dimensions of $7.9 \times 2.6 \times 1.0 \text{ mm}^3$ when in its compressed state (the material's shortest c-axis is aligned in the long direction of the element). It was originally cut by electrical discharge machine and then electropolished in a chilled solution of ethanol (66%) and 16 M nitric acid (34%) to relieve surface stresses. The surface of the element was further treated by shot peening to stabilize a fine twin structure that improves the performance and repeatability of the MSM micropump (Ullakko et al. 2015; Musiienko et al. 2015).

The plastic housing that encases the MSM element (1) (see Fig. 1) consists of three parts and was machined from polycarbonate. The first piece, a base plate (2), has a pocket milled into it slightly larger than the MSM element, measuring $11 \times 3.1 \times 2.3 \text{ mm}^3$. The second piece was

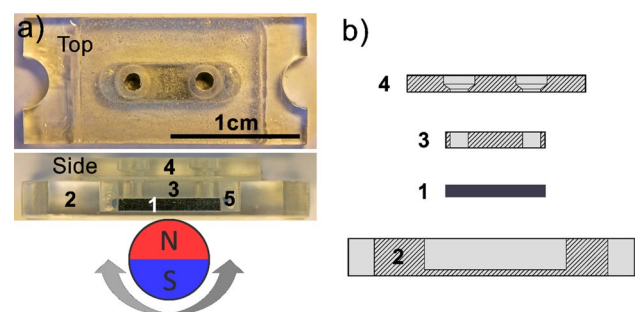


Fig. 1 **a** A top and side view of the MSM micropump. A graphic of the diametrically magnetized cylindrical magnet has been superimposed on the side view for reference, according to the scale. The labeled parts are as follows: (1) MSM element, (2) base plate, (3) inner plate, (4) cover plate and (5) silicone. Note that the encapsulating elastomer layer and mounting epoxy are not clearly visible. **b** Schematic cross-sectional view showing the different parts of the design. The numbering is the same as in **a**

an inner plate (3) measuring $7.8 \times 2.8 \times 1.4 \text{ mm}^3$, which had two holes 1.5 mm in diameter forming the inlet and outlet channels. The third piece (4) was a cover plate, measuring $14 \times 10 \times 1.4 \text{ mm}^3$ with two holes similar to the inner plate. In addition, a 2.5 mm counterbore was drilled into the cover plate to accommodate microfluidic attachments. The purpose of the multi-part design is to constrain the MSM element and minimize the thickness of the elastic material. This results in better sealing of the fluid channel thus greatly improving the pumping characteristics and stability.

The micropump was assembled in a multi-step process. Throughout the process, all components were cleaned with ethanol to ensure there were no contaminants that could inhibit the curing process of any of the resins. The prepared MSM element (1) was centered in the pocket of the base plate (2) and the inner plate (3) placed directly on top of the MSM element. A silicone elastomer (Dow Corning, Sylgard 184) was used to completely encapsulate the MSM element and to create a microfluidic channel. It was poured over the inner plate, filling the pocket of the base plate. Once cured, the elastomer in the holes of the inner plate was removed to clear the microfluidic channel of the micropump. It was determined that the cured elastomer was too stiff to allow for the MSM element to strain along the length of the element which is necessary for the pumping mechanism. As such, the elastomer was removed at both ends of the MSM element to make space for a softer material (labeled as (5) in Fig. 1a). Silicone (Sika, Sikasil-C) was used to fill in this empty space at the ends. The stiffer elastomer remained between the MSM element and the plastic parts on the top, bottom and lateral sides, providing the needed sealing of the fluid channel. Similar to the design by Smith et al. (2015), the fluid channel is formed between the stiffer silicone elastomer–MSM element interfaces during actuation.

A two-part epoxy (Rexxan AG) was applied to the edges of the inner plate (3) to fix it in place. Once cured and grinded, the cover plate (4) was placed on the assembly with the holes concentrically aligned with the holes of the inner plate and held in place with a two-part epoxy. Once cured, the construction of the MSM micropump is complete. The results presented in this paper are from multiple MSM pumps manufactured using these methods.

The feasibility of the MSM micropump to be integrated into planar LoC devices was tested by developing a proof-of-concept linear design. In this design, an MSM element ($0.5 \times 2.6 \times 4.4 \text{ mm}^3$) prepared similarly to the MSM micropump was set with elastomer in a pocket milled into a 1.32 mm sheet of polycarbonate. Instead of the inlet and outlet being located on the top face of the MSM element, they were oriented axially to it to demonstrate a two-dimensional, linear design. The milled channels were sealed with a self-adhesive film. Figure 2 shows a photograph of the prototype using this planar geometry. The rectangular hole

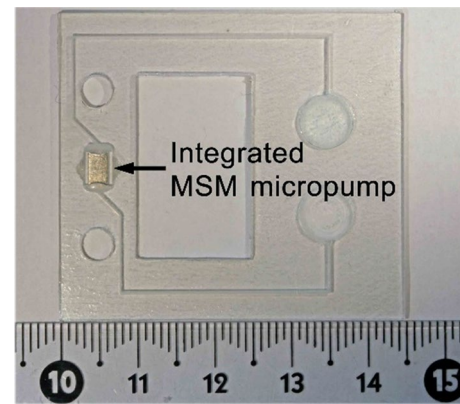


Fig. 2 A prototype of the MSM pump utilizing linear design to demonstrate the integration into a planar architecture

in the middle is to support this linear design on the magnetic fixture and could be avoided.

2.2 Actuation and characterization of the MSM micropump

The MSM micropump works similarly to the swallowing mechanism of animals. The MSM material locally morphs into a cavity when subjected to a heterogeneous magnetic field generated by a diametrically magnetized cylindrical magnet. The cavity formed along the MSM element follows a pole of the magnetic field. Thus, axially rotating the permanent magnet changes the orientation of the magnetic poles and repositions the cavity, moving it continuously from one end of the element to the other. This cavity follows the poles in the direction the magnet is being rotated. Providing the MSM element is in a sealed channel, this cavity can transport fluid from an inlet, located on one end of the element, to an outlet located on the other end. This works analogously to a peristaltic pump. An important property of the MSM micropump is that the direction of the flow can be reversed by changing the direction the magnet is being rotated. Further details regarding the material properties and the pumping mechanism can be found in Aaltio et al. (2016), Smith et al. (2015) and Ullakko et al. (2012).

In the current design, the MSM element is in direct contact with the pumped fluid. The corrosive properties of the MSM alloys were deeply investigated by Liu et al. (2003), Stepan et al. (2007), Gebert et al. (2009) and Pouponneau et al. (2011). Where the corrosive properties of the MSM alloy do not meet the requirements of a particular application, the element has to be coated to prevent direct contact with the pumped fluids. In addition of its chemical compatibility, the coating should have an appropriate strain to follow the MSM element's strain.

A diametrically magnetized cylindrical magnet (NdFeB N52, 6.35 mm OD \times 25.4 mm) with magnetic field measured to be 0.61 T at the magnet's surface was used to actuate the MSM micropump. Magnetic field decays sharply from the surface of the magnet. Because the actuation mechanism lies upon magnetic interaction of the ferromagnetic MSM element with highly inhomogeneous field produced by the magnet, the size of the magnet, its grade and distance between the magnet and the MSM element would affect the pumping characteristics. In the present research, the distance from the magnet's surface to the MSM element was kept around 0.5–0.6 mm. A variation of the distance of \sim 0.1 mm from the magnet to the element produced up to 8% variation in flow rate.

An experimental fixture was developed that held the MSM micropump in place near the permanent magnet and automated the research. The magnet was attached to a 6 W DC motor (Maxon Motor AG, A-Max 22) via a custom aluminum coupler, and an optical encoder (Honeywell, HOA7720-M11) measured the angular frequency of the motor. As there are two poles to a magnet, one revolution of the magnet equates to two pumping cycles. Throughout this paper, the frequency reported refers to the pumping frequency and not the motor frequency. National Instruments DAQs (USB-6002 and USB-6361), in conjunction with custom LabVIEW modules which implemented closed-loop feedback, measured the various sensors used in the experiments and controlled the motor speed.

A separate experimental fixture was created to characterize the pulsatile flow of the MSM micropump. A similar magnet as above was attached to a 1.5° stepper motor (Faulhaber AM1524) to precisely actuate the MSM micropump at pumping frequency of about 2 Hz. The flow generated at this speed was measured using a microfluidic flow rate meter (Sensirion SLI-1000). Due to a relatively slow response time of \sim 40 ms, these measurements give only a qualitative view of the actual flow rate. Thus, other experiments described hereafter were conducted to more precisely measure the flow rate and volume per single pumping cycle.

The MSM micropump is self-priming and can pump gases as well as liquids. The air flow rate was measured by attaching two transparent pipettes to the micropump inlet and outlet. A small drop of water was placed in each of the pipettes which trapped a volume of air of \sim 1 mL between the inlet, pumping channel and outlet. The pump was operated at a constant frequency, f , measured at 20 Hz intervals. The number of pumping cycles, N , needed to move the water droplet through the pipette, Δh , was recorded to calculate the air flow rate, Q_{air} , using Eq. (1), where S is the cross-sectional area of the pipette:

$$Q_{\text{air}} = \frac{\Delta h \times S}{N} f. \quad (1)$$

These measurements were repeated when the direction of flow was reversed. An average volume per cycle was calculated by dividing the flow rate by the pumping frequency maintained within \pm 1 Hz accuracy.

The liquid flow rate of the MSM micropump was measured in a similar way, with a known volume of water, V , of 0.5 mL, being pumped by the pump from one pipette to the other. The number of cycles, N , needed to pump the water to the other pipette, was recorded. Measurements were conducted at multiple pumping frequencies starting at 20 Hz and increasing in 20 Hz increments up to 320 Hz. A similar set of measurements was conducted when the direction of flow was reversed to compare the performance of the pump in either direction. Equation 2 calculates the flow rate of water, Q_{water} , in these experiments:

$$Q_{\text{water}} = \frac{V}{N} f. \quad (2)$$

The precision of the MSM micropump was measured by pumping water repeatedly under the same conditions and then comparing the variance between the measured results. Using the custom software controlled apparatus, the MSM micropump was operated at a constant frequency for a fixed number of cycles across each set of measurements. Ten measurements were conducted at each frequency tested. The volume of water pumped was measured by water mass transferred by the MSM micropump via microfluidic tubing to a precision scale that had an accuracy of 0.03 mg (A&D GH-202). The flow rate of water was calculated using Eq. (2) with volume obtained from the mass measurements: $V = \Delta m / \rho$, where Δm is the difference between mass measurements before and after the experiment, and ρ is the density of water at room temperature.

The downstream backpressure that could be generated by the MSM micropump was measured using a piezoresistive silicon pressure sensor (Honeywell, SSCDANT150PGA5). The inlet of the micropump was connected to a reservoir at ambient pressure with a microfluidic flow rate sensor (Sensirion, SLI-1000) connected inline, and the outlet was connected to a closed volume with the pressure sensor attached. The micropump was operated at a constant frequency and the downstream pressure measured as a function of time. In order to diminish errors in the flow rate measurements caused by the pulsating flow, we connected a simple custom flow pulsation dampener between the pump inlet and the flow rate meter. The measurement continued until the micropump could no longer move the water against the backpressure of the outlet. Additional measurements were conducted at 20 Hz to determine the maximum pressure that the pump could operate against. In this case, the MSM micropump was clamped to create additional compressive force on the MSM element, therefore creating a tighter seal within the microfluidic channel.

The efficacy of the micropump as a valve, operating at standard conditions, was also studied by measuring the flow rate and differential pressure as a function of time. During this experiment, the micropump was actuated at 20 Hz. Once the flow rate stabilized, the chamber valve was closed. The pump was actuated until the backpressure stabilized and the flow rate became near zero. The pump was then stopped with the magnet poles being parallel to the MSM element inside the pump, thus closing the pumping channel. The decrease in pressure was measured in this configuration until it stabilized. The pump was then actuated slowly, at 0.16 Hz, to actuate the pumping channel between its open and closed configurations. The pressure drop and corresponding flow rate were then measured.

All reported measurements were conducted at room temperature.

3 Results and discussion

3.1 Pumping performance

Figure 3 shows the measured time dependence of the MSM micropump’s flow rate when operated at a pumping frequency close to 2 Hz. Each pumping cycle can be clearly seen as distinct pulses with near-zero flow rate between them. This peristaltic motion indicates both discrete resolution and precise dosing. The volume pumped per cycle is dependent mainly on the cross section of the MSM element (e.g., for a cross section of $1 \times 2.5 \text{ mm}^2$, the volume per cycle is $\sim 110\text{--}130 \text{ nL}$). Since the MSM micropump is scalable, the volume per cycle can be tailored specific to the application. The profiles of each pulse are very similar, but due to the measuring delay in the sensor, absolute flow rate and repeatability characteristics cannot be inferred from these data.

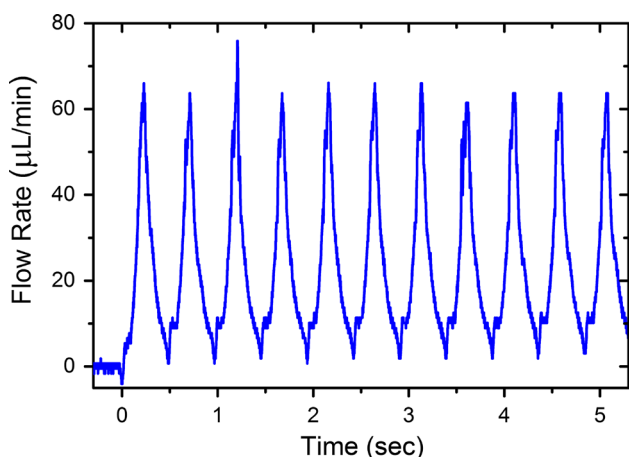


Fig. 3 Pulsating flow rate generated by the MSM micropump at a pumping frequency of $\sim 2 \text{ Hz}$

Figure 4 shows the results of the flow rate experiments. Results are given for both water and air pumped in either direction. In the figure, the flow rate of the air experiments (circles and squares) follow a quasi-linear fit through the origin which indicate that the volume pumped per cycle is consistent across a wide range of frequencies. The volume pumped per cycle for air is $140 (125) \pm 5 \text{ nL}$ for the forward (reverse) direction. The flow rate of the water experiments (down and up triangles) follows a parabolic fit through the origin. The volume of water pumped per cycle starts at $135 (120) \pm 3 \text{ nL}$ in the forward (reverse) direction at 20 Hz, but gradually decreases to $105 (85) \pm 3 \text{ nL}$ in the forward (reverse) direction at 320 Hz.

The small difference in performance between pumping directions is related to hysteresis properties of the MSM material leading to asymmetry in the cavity shape for different directions. The decrease in the volume of water pumped per cycle at increasing frequencies can be explained by the geometry of the cavity that carries the fluid which has an approximate depth of $30 \mu\text{m}$ (Smith et al. 2015). Thus, surface effects, such as wettability, and viscosity begin to dominate the microfluidic dynamics at these dimensions and pumping speeds. Were the pumping frequency increased further, we hypothesize the flow rate for water would approach an asymptotic maximum. The effect of viscosity was observed earlier with a 60 wt% glycerol solution, having a viscosity approximately 10 times greater than water, where an asymptotic maximum occurred at $\sim 250 \text{ Hz}$ pumping frequency (Smith et al. 2015).

Figure 5 presents the results of the repeatability tests. Water was pumped at frequencies between 20 and 50 Hz at 10 Hz intervals, for a fixed amount of pumping cycles

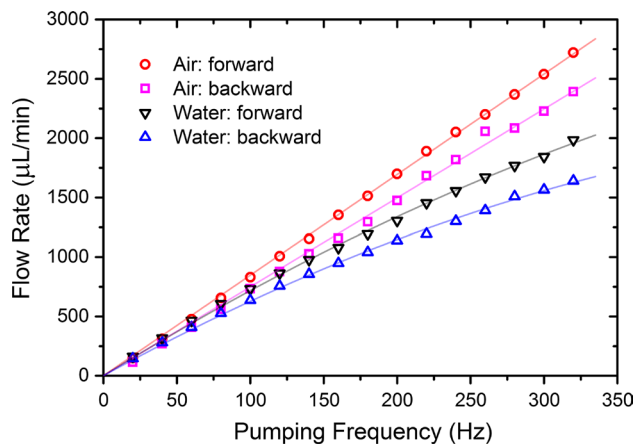


Fig. 4 Flow rate of the MSM micropump as a function of pumping frequency (no back pressure applied), for both pumping directions. The flow rate of the air pumped (circle and square) follows a linear trend whereas the flow rate of the water (down triangle and up triangle) follows a parabolic trend. The effects of wettability and viscosity lead to a decrease in flow rate for water at elevated frequencies

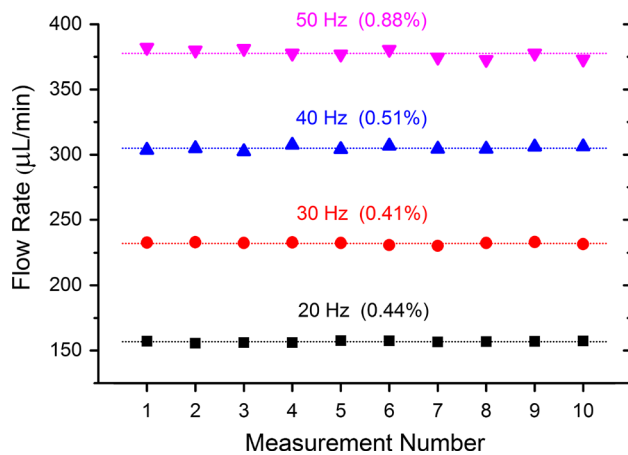


Fig. 5 Results of multiple flow rate tests conducted at various frequencies used to determine the repeatability of the MSM micropump. Each measurement consists of 1001 ± 1 pumping cycles, which corresponds to ~ 0.13 mL pumped volume. The frequency and variability of each set of data is included in the graph. Dotted lines show the mean values for each set of data

($N = 1001 \pm 1$) in each measurement. The standard deviation was calculated for each set of frequency-dependent data, to determine the consistency in which the pump performed between tests. At 20 Hz, the flow rate varied by 0.41%. The variance increased to 0.88% at 50 Hz. These results demonstrate that the volume pumped per cycle is very consistent when using the same pumping parameters. This exceptional precision is one reason why this version of the MSM micropump is superior to previous designs. Under constant conditions, the MSM material responds to the applied magnetic field by generating the same cavity geometry each cycle. A less constraining environment allows for a dynamic change in the pumping conditions. This would affect the physical response of the material to the magnetic field, thus altering the volume pumped per cycle and decreasing the instrument precision. Constraining the MSM element creates a static environment that improves the performance of the micropump.

Figure 6 shows the relationship between the flow rate and downstream backpressure of the MSM micropump when operated at different frequencies. The micropump generated pressure within the closed volume which, in turn, suppressed the flow rate. The flow rate decreases with increasing backpressure, reaching 0 $\mu\text{L}/\text{min}$ at 3.25 bar when operated at 10 Hz and 4.5 bar when operated at 80 Hz. Zero flow rate does not mean that we have no transfer of fluid, but rather that there is a leakage in the pump sealing. At this point, the pump is actively transporting liquid to the outlet via the cavity, but equal amounts are forced back through the inlet (backflow) in between, or during, active pulses. This was verified by observing a pressure drop when the pump was stopped.

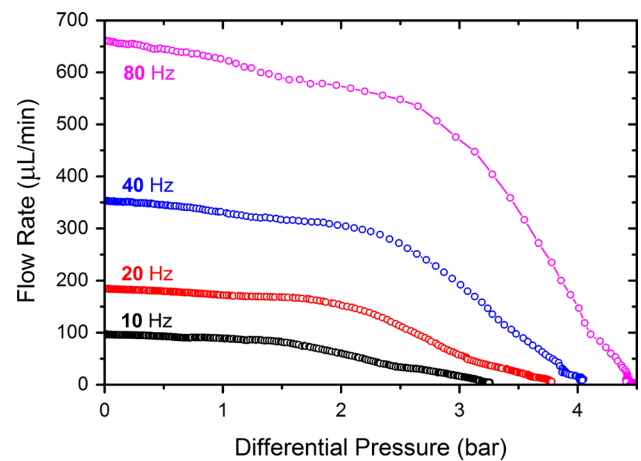


Fig. 6 Flow rate versus differential (back) pressure dependencies measured at different pumping frequencies for the MSM micropump

Figure 7 illustrates the differential pressure and corresponding flow rate of the micropump, as a function of time. The pump was actuated at $t = 0$, at 20 Hz pumping frequency, and the flow rate stabilized at $t \sim 18$ s. The chamber valve was then closed, and the pump generated a differential pressure of 3.76 ± 0.02 bar. At 145 s, the pump was stopped with the pump channel in its closed position. The pressure dropped 0.03 bar over 55 s in this configuration. The pump was then actuated five times at 0.16 Hz to open and close the pump channel. Large negative spikes, indicating the pump channel

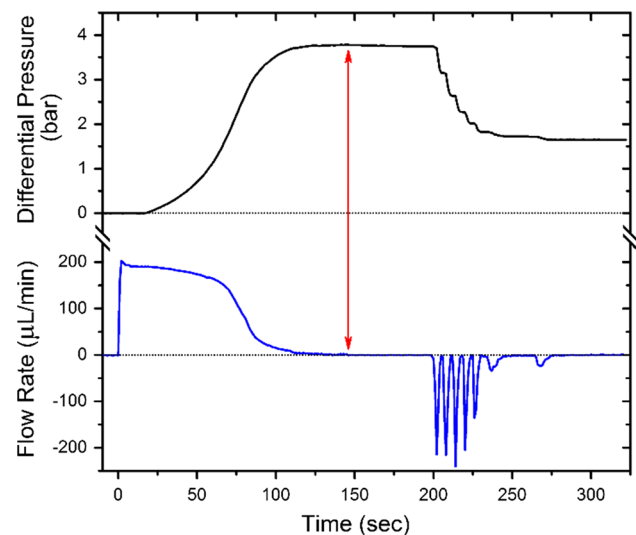


Fig. 7 Differential pressure and flow rate as functions of time for an MSM micropump. Pressure was generated by actuating the pump at 20 Hz until a maximum pressure of 3.76 bar was achieved. The pump was stopped at 145 s (see the arrow) and left in the closed position. Negligible leakage was detected until the pump was slowly actuated at 200 s. The pressure drop and corresponding negative spikes in flow rate indicate leakage through the pump channel when the pump channel was open

was open, can be seen in the flow rate which correspond to pressure drops. The last two spikes correspond to manual rotation of the magnet and are not equalized in time with the previous five. The pressure stabilized at 1.64 ± 0.01 bar with no pressure decrease detected during the last 45 s of the experiment. These results demonstrate that the MSM micropump simultaneously acts a closed valve which cannot be opened at low pressures.

Figure 8 shows the pressure generated by the MSM micropump as a function of time when it was operated at a constant frequency of 20 Hz under an additional compressive force. The pressure within the closed volume increased to 10 bar within 4.5 min. These data were further analyzed to determine the pumping characteristics as a function of backpressure, with the calculation results shown in the inset. The flow rate was estimated based on Boyle's law, taking into account the known volume of the chamber and ambient pressure. According to this calculation, the pump performed consistently up to a backpressure of ~ 1.5 bar. At this pressure, the flow rate began to decrease almost linearly as a function of the backpressure, resulting in a maximum pressure of 10 bar being generated when the flow rate was reduced to zero. This is a significant improvement compared to previous pumps which could not generate more than 1.5 bar of pressure (Smith et al. 2015). Furthermore, this is substantially closer to the theoretical limit of 20 bar which is the blocking stress where the MSM material will no longer strain from a magnetic field (Murray et al. 2001). These results indicate that the maximum pressure the MSM micropump can generate, strongly correlates to the quality of the seal. Throughout these experiments, the power required to operate the MSM micropump was measured in a similar method as Smith et al. (2015). The power consumed by the

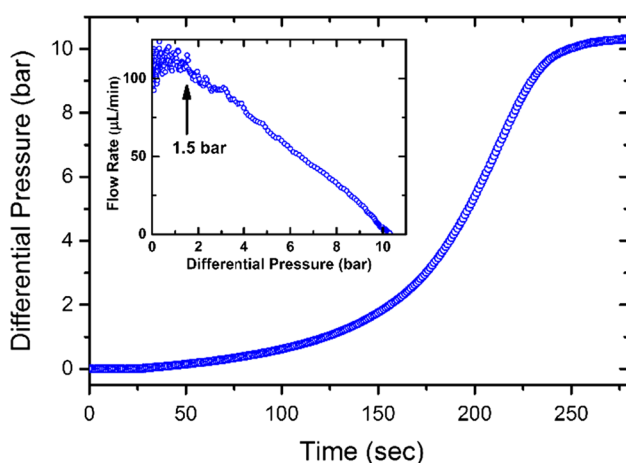


Fig. 8 The pressure generated by the MSM micropump, at 20 Hz, as a function of time. Inset: the flow rate stays approximately constant up to a pressure of 1.5 bar and then decreases until it no longer pumps at 10 bar

MSM micropump was 0.8 ± 0.05 mJ/cycle, without changes during the measurement, even at the maximum pressure.

3.2 Integration into lab-on-a-chip

In addition to its technical performance, the MSM micropump has characteristics that make it a highly competitive flow control solution for PoCD and LoC technologies. One such characteristic is the simplicity and modularity of its design. Mechanical parts, such as valves and diaphragms, and electrical connections significantly increase the intricacy of micropump technologies, complicating their integration into microfluidic platforms. The MSM micropump utilizes an advanced magnetic material which controls the flow of fluid and simultaneously acts as a valve, preventing backflow. A magnetic field actuates this material, thereby removing the need for electrical contacts interfacing with the microfluidic device.

For systems with integrated sensors and control electronics, the external magnetic field produced by the rotating permanent magnet should be taken into account. The maximum field measured close to the magnet's surface reaches 610 mT and decreases down to 10 mT at a distance of 15–20 mm from the magnet's center. The length of the magnet can be reduced to $\sim (1.2\text{--}1.5) \times W$, where W is the width of the MSM element. From these data, one can conclude that the integrated sensors/electronics should be arranged at a proper distance from the magnet, according to their requirements. In addition, magnetic shielding materials (such as high magnetic permeability metal alloys or ferromagnetic metal coatings) can be used to effectively draw the field away from the sensitive devices.

The linear micropump design, shown previously in Fig. 2, demonstrates proof-of-concept of one method of how the MSM micropump could be integrated into PoCD and LoC technologies. Figure 9 illustrates the flow rate, when pumping water, of this integrated MSM micropump as a function of frequency. The change in the flow rate decreases with increasing frequency, nearing an asymptotic value of 260 $\mu\text{L}/\text{min}$ at 150 Hz. At 50 Hz, where both the flow rate versus frequency for the original design and integrated design is relatively linear, the flow rate is 380 and 160 $\mu\text{L}/\text{min}$, and calculated volume per cycle is 127 and 53 nL, respectively. The difference between these flow rates at 50 Hz is largely accounted for the 50% difference in the cross section of the MSM element in each case. However, a key difference with the integrated pump is that it reaches an asymptotic value much earlier compared to the original design. We hypothesize that the interface with the microfluidic channel and the cavity is substantially smaller for the integrated micropump (in this case, $\sim 15 \mu\text{m} \times 2.6 \text{ mm}$) rather than the inlet interfacing with the entire face of the cavity as in the original design. Further work is needed on the integrated design for

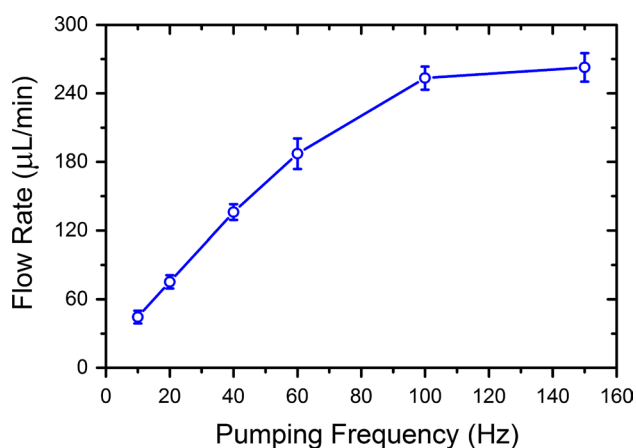


Fig. 9 Flow rate of water versus pumping frequency measured for the integrated linear MSM pump presented in Fig. 2

it to have similar performance to the original design. A video demonstrating this design pumping colored water in both directions, at 20 Hz pumping frequency, can be found online in supplemental materials.

Figure 10 shows a rendered isometric and cross-sectional view of two plausible scenarios that the MSM micropump could be integrated into a LoC or PoCD device. The first, Fig. 10a, is similar to the integrated, inline MSM micropump that is shown in Fig. 2 and was characterized in this paper. In this case, the MSM element is integrated into an arbitrary LoC inline with the microfluidic channel during the manufacturing of the microfluidic device, thereby maintaining the planar geometry of the LoC. Figure 10b illustrates another scenario where a modular MSM micropump can be attached to the LoC. This method is advantageous in that the MSM micropump can be easily distributed to microfluidic device manufacturers and assembled onsite rather than requiring integration during the manufacturing process. An advantage in each of these scenarios is that the MSM micropump is actuated externally by a magnet, shown in the figure. The

design is simple and modular: Only the MSM micropump needs to be integrated into, or with, the microfluidic device or chip, and the magnetic field source and driving electronics can be located separately being a part of an instrument. This significantly reduces the complexity of integrating this technology and reduces the costs associated with disposable PoCD and LoC devices.

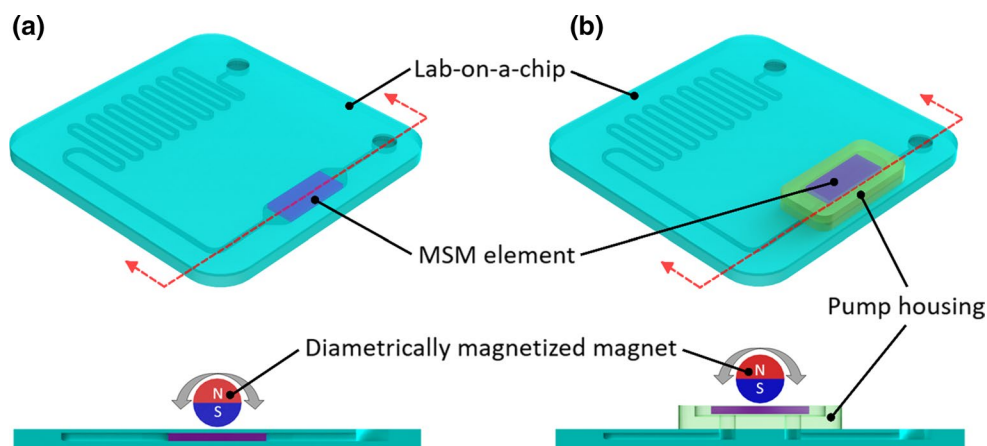
It has been demonstrated that Ni–Mn–Ga evinces the MSM effect even at geometries of only a few micrometers (Musiienko et al. 2017). With more advanced manufacturing techniques, the size of the MSM element could be reduced and integrated directly into the channels of microfluidic technologies. The volume pumped per cycle would change according to the geometry of the MSM element, but we expect similar quality of performance even at a reduced scale. It would be self-priming, pumping both gases and liquids. It could pump against a significant backpressure, and it would offer precise management of nanoscale fluids across a range of flow rates.

4 Conclusions

By applying a magnetic field, a peristaltic-like motion is generated in the magnetic shape memory material Ni–Mn–Ga which is used to repeatedly pump precise quantities of fluid. In this paper, we present a design of the MSM micropump where the MSM element is encapsulated in a constraining environment which enables consistent, stable performance of the pump. This technology is greatly improved compared to the previous reporting of the MSM micropump.

The pumping performance was systematically characterized with air and water, in both directions, and in a wide pumping frequency range. The water flow rate follows a parabolic fit, measured 160 (140) $\mu\text{L}/\text{min}$ in the forward (reverse) direction at 20 Hz pumping frequency, and reaching 2000 (1600) $\mu\text{L}/\text{min}$ at 320 Hz. The nonlinearity is attributed primarily to effects of wettability and viscosity,

Fig. 10 An isometric and cross section rendering of two methods of integrating the MSM micropump into an LoC. **a** The MSM micropump can be integrated directly into the LoC during its manufacturing. **b** The MSM micropump can be modular and attach to the LoC after it has been manufactured



which begin to dominate the microfluidic dynamics at elevated pumping speeds. For air, the flow rate follows a linear fit, proving the pumping mechanism to work equally within the measured frequency range.

The variance in pumping performance has been reduced to ~0.5–0.9%, measured at pumping frequencies 20–50 Hz. The flow rate is stable up to 1.5 bar, and the pump can generate a pressure of more than 4 bar. Additional clamping allows generation of higher pressures, up to 10 bar. Furthermore, the valve properties of the constrained design are substantially improved, holding a consistent pressure of over 3.5 bar.

In addition to its strong technical performance, the MSM micropump is a simple, modular technology. Mechanical parts and electrical contacts found in other micropumps are replaced by an advanced shape memory technology that is controlled by an external magnetic field. This greatly simplifies the process of integrating the MSM micropump directly into microfluidic platforms such as PoCD and LoC devices. We present a proof-of-concept design where the MSM element is directly integrated inline with a microfluidic channel, modeling a potential method of integrating the MSM micropump into planar microfluidic technologies. The second plausible scenario is a modular MSM micropump which can be attached to the microfluidic device after the manufacturing process.

Acknowledgements Janne Huimasalo is thanked for his assistance in manufacturing the micropump and the experimental setup. The Academy of Finland (Grant No. 277996) is acknowledged for the financial support.

References

- Aalto I, Sozinov A, Ge Y, Ullakko K, Lindroos VK, Hannula S-P (2016) Giant magnetostrictive materials. In: Hashmi S (ed) Reference module in materials science and materials engineering. Elsevier, Oxford, pp 1–14
- Barker S, Rhoads E, Lindquist P, Vreugdenhil M, Müllner P (2016) Magnetic shape memory micropump for submicroliter intracranial drug delivery in rats. *J Med Dev* 10:041009. <https://doi.org/10.1115/1.4034576>
- Berg JM, Anderson R, Anaya M, Lahlouh B, Holtz M, Dallas T (2003) A two-stage discrete peristaltic micropump. *Sens Actuators A Phys* 104:6–10. [https://doi.org/10.1016/S0924-4247\(02\)00434-X](https://doi.org/10.1016/S0924-4247(02)00434-X)
- Gebert A, Roth S, Oswald S, Schultz L (2009) Passivity of polycrystalline NiMnGa alloys for magnetic shape memory applications. *Corros Sci* 51:1163–1171. <https://doi.org/10.1016/j.corsci.2009.02.016>
- Guttenberg Z, Müller H, Habermüller H, Geisbauer A, Pipper J, Felbel J, Kielpinski M, Scriba J, Wixforth A (2005) Planar chip device for PCR and hybridization with surface acoustic wave pump. *Lab Chip* 5:308–317. <https://doi.org/10.1039/B412712A>
- Harrison DJ, Manz A, Glavina PG (1991) Electroosmotic pumping within a chemical sensor system integrated on silicon. In: Proceeding of international conference on solid-state sensors and actuators, TRANSDUCERS '91. Digest of technical papers, San Francisco, pp 792–795. <https://doi.org/10.1109/SENSOR.1991.149002>
- Husband B, Bu M, Evans AGR, Melvin T (2004) Investigation for the operation of an integrated peristaltic micropump. *J Micromech Microeng* 14:S64–S69. <https://doi.org/10.1088/0960-1317/14/9/011>
- Jang LS, Kan WH (2007) Peristaltic piezoelectric micropump system for biomedical applications. *Biomed Microdev* 9:619–626. <https://doi.org/10.1007/s10544-007-9075-1>
- Juncker D, Schmid H, Drechsler U, Wolf H, Wolf M, Michel B, de Rooij N, Delamarch E (2002) Autonomous microfluidic capillary system. *Anal Chem* 74:6139–6144. <https://doi.org/10.1021/ac0261449>
- Kai E, Pan T, Ziaie B (2004) A robust low-cost PDMS peristaltic micropump with magnetic drive. In: Conference proceedings of solid-state sensor, actuator and microsystems workshop, pp 270–273
- Laser DJ, Santiago JG (2004) A review of micropumps. *J Micromech Microeng* 14:R35. <https://doi.org/10.1088/0960-1317/14/6/R01>
- Liu XW, Söderberg O, Ge Y, Lanska N, Ullakko K, Lindroos VK (2003) On the corrosion of non-stoichiometric martensitic Ni–Mn–Ga alloys. *J Phys IV Fr* 112:935–938. <https://doi.org/10.1051/jp4:20031034>
- Manz A, Graber N, Widmer HM (1990) Miniaturized total chemical analysis systems: a novel concept for chemical sensing. *Sens Actuators B Chem* 1:244–248. [https://doi.org/10.1016/0925-4005\(90\)80209-i](https://doi.org/10.1016/0925-4005(90)80209-i)
- Murray SJ, Marioni MA, Allen SM, O'Handley RC, Lograsso TA (2000) 6% magnetic-field-induced strain by twin-boundary motion in ferromagnetic Ni–Mn–Ga. *Appl Phys Lett* 77:886–888. <https://doi.org/10.1063/1.1306635>
- Murray SJ, Marioni M, Tello PG, Allen SM, O'Handley RC (2001) Giant magnetic-field-induced strain in Ni–Mn–Ga crystals: experimental results and modelling. *J Magn Magn Mater* 226:945–947. [https://doi.org/10.1016/S0304-8853\(00\)00611-9](https://doi.org/10.1016/S0304-8853(00)00611-9)
- Musiienko D, Smith AR, Saren A, Ullakko K (2015) Stabilization of a fine twin structure in Ni–Mn–Ga by a diamond-like carbon coating. *Scr Mater* 106:9–12. <https://doi.org/10.1016/j.scripamat.2015.03.018>
- Musiienko D, Saren A, Ullakko K (2017) Magnetic shape memory effect in single crystalline Ni–Mn–Ga foil thinned down to 1 μm . *Scr Mater* 139:152–154. <https://doi.org/10.1016/j.scripamat.2017.06.027>
- Nguyen NT, Huang X, Chuan TK (2002) MEMS-micropumps: a review. *J Fluids Eng* 124:384–392. <https://doi.org/10.1115/1.1459075>
- Pečar B, Križaj D, Vrtačnik D, Resnik D, Dolžan T, Možek M (2014) Piezoelectric peristaltic micropump with a single actuator. *J Micromech Microeng* 24:105010. <https://doi.org/10.1088/0960-1317/24/10/105010>
- Pouponneau P, Savadogo O, Napporn T, Yahia LH, Martel S (2011) Corrosion study of single crystal Ni–Mn–Ga alloy and Tb_{0.27}Dy_{0.73}Fe_{1.95} alloy for the design of new medical micro-devices. *J Mater Sci Mater Med* 22:237–245. <https://doi.org/10.1007/s10856-010-4206-2>
- Saren A, Musiienko D, Smith AR, Ullakko K (2016) Pulsed magnetic field-induced single twin boundary motion in Ni–Mn–Ga 5M martensite: a laser vibrometry characterization. *Scr Mater* 113:153–157. <https://doi.org/10.1016/j.scripamat.2015.10.020>
- Sheen HJ, Hsu CJ, Wu TH, Chang CC, Chu HC, Yang CY, Lei U (2008) Unsteady flow behaviors in an obstacle-type valveless micropump by micro-PIV. *Microfluid Nanofluidics* 4:331–342. <https://doi.org/10.1007/s10404-007-0189-9>
- Smith A, Tellinen J, Müllner P, Ullakko K (2014a) Controlling twin variant configuration in a constrained Ni–Mn–Ga sample

- using local magnetic fields. *Scr Mater* 77:68–70. <https://doi.org/10.1016/j.scriptamat.2014.01.028>
- Smith AR, Tellinen J, Ullakko K (2014b) Rapid actuation and response of Ni–Mn–Ga to magnetic-field-induced stress. *Acta Mater* 80:373–379. <https://doi.org/10.1016/j.actamat.2014.06.054>
- Smith AR, Saren A, Järvinen J, Ullakko K (2015) Characterization of a high-resolution solid-state micropump that can be integrated into microfluidic systems. *Microfluid Nanofluid* 18:1255–1263. <https://doi.org/10.1007/s10404-014-1524-6>
- Smits JG (1990) Piezoelectric micropump with three valves working peristaltically. *Sens Actuators A Phys* 21:203–206. [https://doi.org/10.1016/0924-4247\(90\)85039-7](https://doi.org/10.1016/0924-4247(90)85039-7)
- Sozinov A, Likhachev AA, Lanska N, Ullakko K (2002) Giant magnetic-field-induced strain in NiMnGa seven-layered martensitic phase. *Appl Phys Lett* 80:1746–1748. <https://doi.org/10.1063/1.1458075>
- Stepan LL, Levi DS, Gans E, Mohanchandra KP, Ujihara M, Carman GP (2007) Biocorrosion investigation of two shape memory nickel based alloys: Ni–Mn–Ga and thin film NiTi. *J Biomed Mater Res* 82A:768–776. <https://doi.org/10.1002/jbm.a.31192>
- Stone HA, Stroock AD, Ajdari A (2004) Microfluidics toward a lab-on-a-chip. *Annu Rev Fluid Mech* 36:381–411. <https://doi.org/10.1146/annurev.fluid.36.050802.122124>
- Tellinen J, Suorsa I, Jääskeläinen A, Aaltio I, Ullakko K (2002) Basic properties of magnetic shape memory actuators. In: Borgmann H (ed) Proceedings of 8th international conference on new actuators, actuator. Messe Bremen GMBH, Bremen, pp 566–569
- Ullakko K, Likhachev AA (2000) Magnetic-field-controlled twin boundaries motion and giant magneto-mechanical effects in Ni–Mn–Ga shape memory alloy. *Phys Lett A* 275:142–151. [https://doi.org/10.1016/S0375-9601\(00\)00561-2](https://doi.org/10.1016/S0375-9601(00)00561-2)
- Ullakko K, Huang JK, Kantner C, O’Handley RC, Kokorin VV (1996) Large magnetic-field-induced strains in Ni₂MnGa single crystals. *Appl Phys Lett* 69:1966. <https://doi.org/10.1063/1.117637>
- Ullakko K, Wendell L, Smith A, Müllner P, Hampikian G (2012) A magnetic shape memory micropump: contact-free, and compatible with PCR and human DNA profiling. *Smart Mater Struct* 21:115020. <https://doi.org/10.1088/0964-1726/21/11/115020>
- Ullakko K, Chmielus M, Müllner P (2015) Stabilizing a fine twin structure in Ni–Mn–Ga samples by coatings and ion implantation. *Scr Mater* 94:40–43. <https://doi.org/10.1016/j.scriptamat.2014.09.013>
- Wang Z, Jian Z (2011) Recent advances in particle and droplet manipulation for lab-on-a-chip devices based on surface acoustic waves. *Lab Chip* 11:1280–1285. <https://doi.org/10.1039/C0LC00527D>
- Webster JR, Burns MA, Burke DT, Mastrangelo CH (2000) Electrophoresis system with integrated on-chip fluorescence detection. In: Proceedings of 13 international conference on micro electro mechanical systems (Cat. No. 00CH36308), Miyazaki, pp 306–310. <https://doi.org/10.1109/MEMSYS.2000.838534>
- Whitesides GM (2006) The origins and the future of microfluidics. *Nature* 442:368–373. <https://doi.org/10.1038/nature05058>
- Zimmermann M, Schmid H, Hunziker P, Delamarque E (2006) Capillary pumps for autonomous capillary systems. *Lab Chip* 7:119–125. <https://doi.org/10.1039/B609813D>